Supplement of Atmos. Meas. Tech., 15, 1093–1105, 2022
https://doi.org/10.5194/amt-15-1093-2022-supplement

Atmospheric Measurement Techniques
Open Access
EGU

Supplement of

Laser imaging nephelometer for aircraft deployment

Adam T. Ahern et al.

Correspondence to: Adam T. Ahern (adam.ahern@noaa.gov)

Figure S1 shows a schematic of the laboratory setup for calibrating the Laser imaging nephelometer (LiNeph). In this configuration, the sample volume of the LiNeph can be evacuated and back-filled with calibration gases, either He or CO_2. Alternatively, calibration aerosol may be introduced via positive pressure from a compressed zero air cylinder by removing the pump from the system and allowing the LiNeph to exhaust through the filter into the room.

Figure S2, S3, S4, and S5 show a comparison of measured differential scattering coefficients (σ°) and calculations from Mie theory. In the bottom panels, two Mie theory calculations of I_{scat} are shown to evaluate the magnitude of the scattering plane rotation shown in Fig. 1b as η. The calculations are based on Equations 81 and 82 from Dolgos (2014),

$$I_{scat,j}(\theta) \propto \beta_{scat} * (P_{11}(\theta) + (P_{12}(\theta) * q_j^{in}(\theta))) \quad \text{(S1)},$$

where $I_{scat,j}$ is the radiance observed by the detector j (i.e. "Perp" or "Para"), β_{scat} is the integrated scattering coefficient, P_{11} and P_{12} are scattering matrix elements, and q_j^{in} is the second Stokes parameter for the incident light in the scattering plane. When the central axis of the wide angle lens is aligned with the polarization of the laser, q_j^{in} equals q_j. However, because of the small offset that allows for two wavelengths to be measured simultaneously, the rotation of the scattering plane must be accounted for using,

$$q_j^{in}(\theta) = q_j * cos\left(2\eta^{\theta,j}\right) + u_j * sin\left(2\eta^{\theta,j}\right) \quad \text{(S2)},$$

where q_j and u_j are the Stokes parameters for the light as defined by the lasers' polarization plane. η is the angle, in the scattering plane that is created by the offset of the lasers from the wide angle lens' central axis. In the first calculation of $I_{scat,j}(\theta)$, shown as a gold line in S2-S5, we assume that η is zero, which results in $I_{scat,j}$ as shown in Eq. 4 and 6.

For the second calculation, we use an estimated η, shown in the top-most panels of S2 and S3. We estimated η by first locating the origin pixel on the CCD array for each camera using an imaged grid. Once we knew the origin pixel row location, we applied the same angular scattering calibration that we found using PSLs to the pixel row (instead of the pixel column). We believe this to be a reasonable estimate given the radially symmetric nature of the wide angle lens, the square shape of the CCD pixels, and the mounting orientation of the CCD. We can then estimate η using the peak location of the Gaussian fit for each CCD orientation, j. The top-most panels of S2 and S3 show that this estimate of η is a function of the detector geometry, j, and scattering angle, θ. For this work, we optimized the laser alignment, which changes the laser position and therefore η, to minimize background light in the instrument. In future work, it would be prudent to minimize η to the extent practical, or else ensure that η is the same for both "Para" and "Perp" detectors.

Figure S6 shows the scattering angle calibration performed by matching maxima and minima observed in measured scattering intensity to the maxima and minima predicted by Mie theory. The calibration aerosol were atomized and dried polystyrene latex spheres of known sizes.

Figure S7 shows a series of measurements of pure CO_2. For this experiment, the LiNeph chamber was filled with CO_2 and then a series of images were captured. From these images, the He image was subtracted. Gaussian fits were applied to each pixel column. Figure S7 shows the area under that Gaussian fit for each image as a function of time for an individual pixel column, which corresponds to a scattering angle.

Figure S8 shows the standard deviation for the area under fitted Gaussian curves as a function of the average area under Gaussian curves for CO_2 measurements. The two traces show different exposure durations and have been normalized by CCD exposure time to be proportional to scattering intensity instead of the digital output. The spread in the data points is from additional noise due to stray light within the instrument. This illustrates that for measurements with abundant signal, the standard deviation is typically <2% of the average signal. But in cases of low signal, the standard deviation becomes constant ~200 bits, and uncertainty is likely dominated by electronic noise. Since phase functions can span many orders of magnitude, we find it advantageous at times to increase the exposure time of the CCD, which linearly increases the signal while the electronic noise remains the same. The resulting Gaussian fit values can be scaled by their exposure time and recombined, allowing for more precise measurements of phase functions spanning multiple orders of magnitude.

Figure S9 shows the sum of all pixels while sampling a well-mixed smoke plume during FIREX-AQ. The red colored region indicates the period of the sampling when a filter is in the sampling line. Only the steady-state data points of the red region are used to correct for changing gas-phase scattering and instrument background light.

Figure S10 shows a subset of the plot on the right side of Fig. 6, showing only the data where the bridge dilution system was not being used, see Fig. 3. The greater linearity between the integrated scattering measured by the LiNeph and the AOP instrument suite for undiluted data compared to all data is consistent with the dilution system being an added source of uncertainty. This plot also indicates that there may be an error in the magnitude of the differential scattering calibration which results in the LiNeph measuring 20-30% more light scattering than what is observed by the AOP instrument suite. We do not expect this to influence the polarimetry measurements as they are normalized functions.

Figure S11 markers show the average normalized number-weighted size distributions for two transects during the Williams Flats Fire on August 7th, 2019. Each size distribution was first normalized by its maximum peak height. Then the average and standard deviation of each size bin was calculated for all the normalized size distributions from each transect. Size distributions were measured using the LAS with an ammonium sulfate calibration as discussed in Moore et al. (2021). Additionally, we fit each individual size distribution with a lognormal distribution and then calculated the average and standard deviation of the fitted mode. Transect 1 had an average mode of 0.174 ± 0.014 μm and Transect 10 had an average mode of 0.225 ± 0.011 μm.

Figure S12 shows the asymmetry parameter (g) as calculated by MiePlot for various theoretical aerosol populations (Laven, 2003). We varied the complex refractive index and the mode of the lognormal distribution to simulate what effect a non-zero η will have on the asymmetry parameter measured by the LiNeph for different aerosol populations. The x-axis shows the g for $\eta = 0$. The y-axis shows the g that is calculated when the upper limit of η used to calculate to the $\sigma°$ observed by each detector. We then use the $\sigma°$ to calculate P_{11} (incorrectly assuming $\eta = 0$) to evaluate the error that might be introduced by neglecting to account for η when calculating g. We see that for a mode diameter of 200 nm, changing the complex refractive index induces

small changes in g, and that the potential bias from η is about 2% for λ = 660 and 405 nm, albeit with different signs. As the mode diameter changes, the sign of the bias can change, but for the cases we examined the bias does not exceed a magnitude of 5%.

Dolgos, G.,: Polarized Imaging Nephelometer Development and Applications on Aircraft, Doctor of Philosophy, Physics, University Maryland Baltimore County, 2014.

Laven, P.: Simulation of rainbows, coronas, and glories by use of Mie theory, Appl. Optics, 42, 436–444, https://doi.org/10.1364/AO.42.000436, 2003.

Laven, P.: MiePlot, available at: http://www.philiplaven.com/mieplot.htm, last access: 14 Oct 2021.

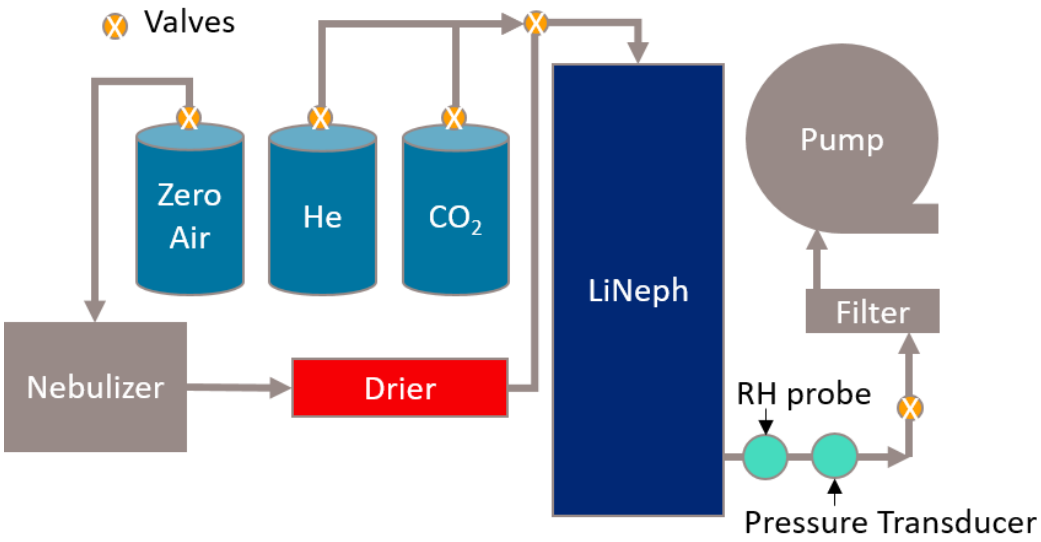

Figure S1. Diagram of laboratory calibration of Laser Imaging Nephelometer.

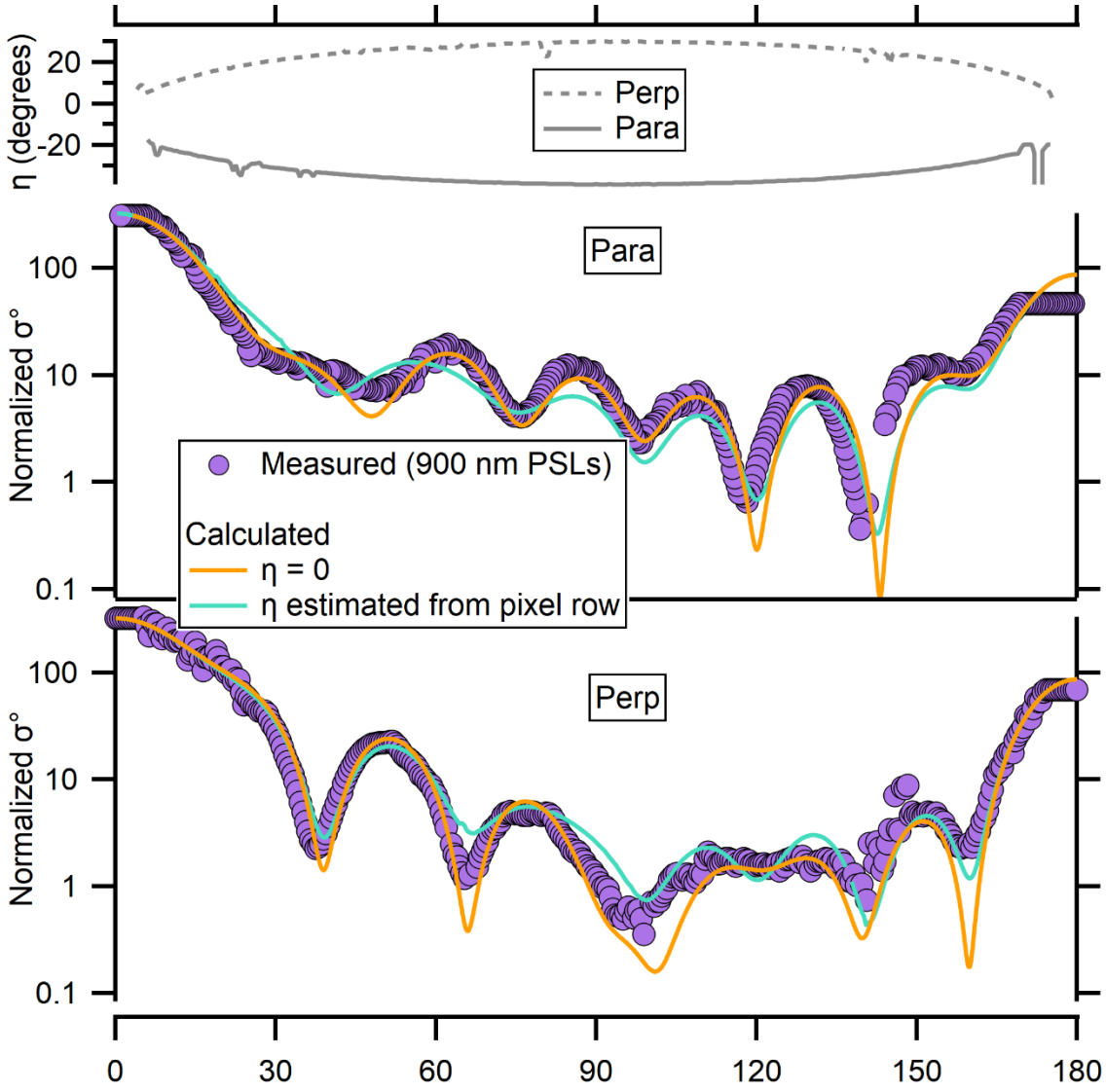

Figure S2. Comparison of measured versus calculated differential scattering coefficient (σ°) of 900 nm PSLs for λ = 405. a) Dashed (solid) lines show the estimated scattering plane rotation (η) based on pixel row for 405 nm laser as viewed by the "Perp" ("Para") oriented CCD. b) Markers show the measured σ°, the solid lines show the σ° calculated using Mie theory. The gold lines were calculated assuming η = 0 and the green were calculated using an estimate of η.

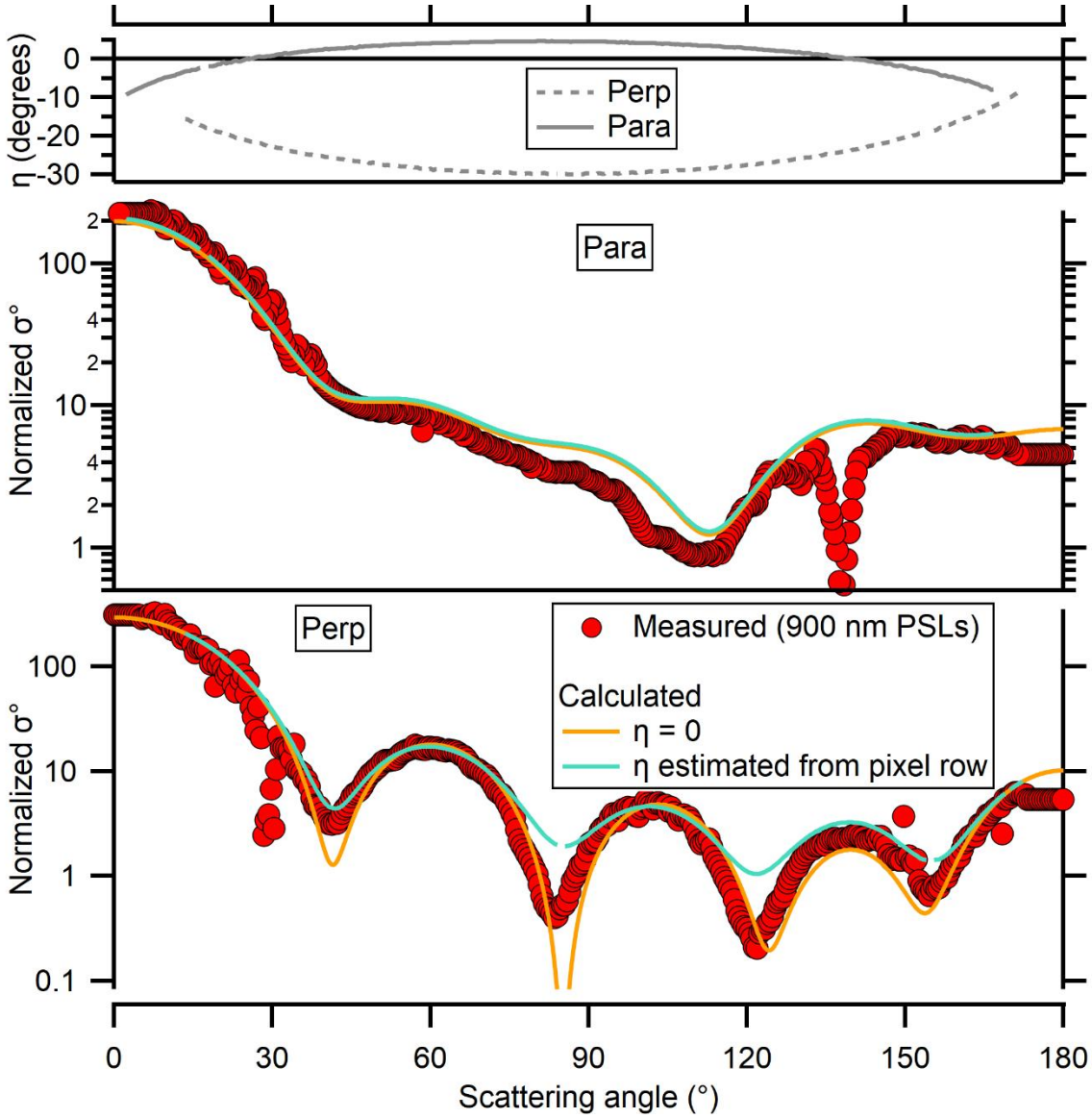

Figure S3. Same as 2 but for λ = 660 nm and PSLs with D_p = 900 nm.

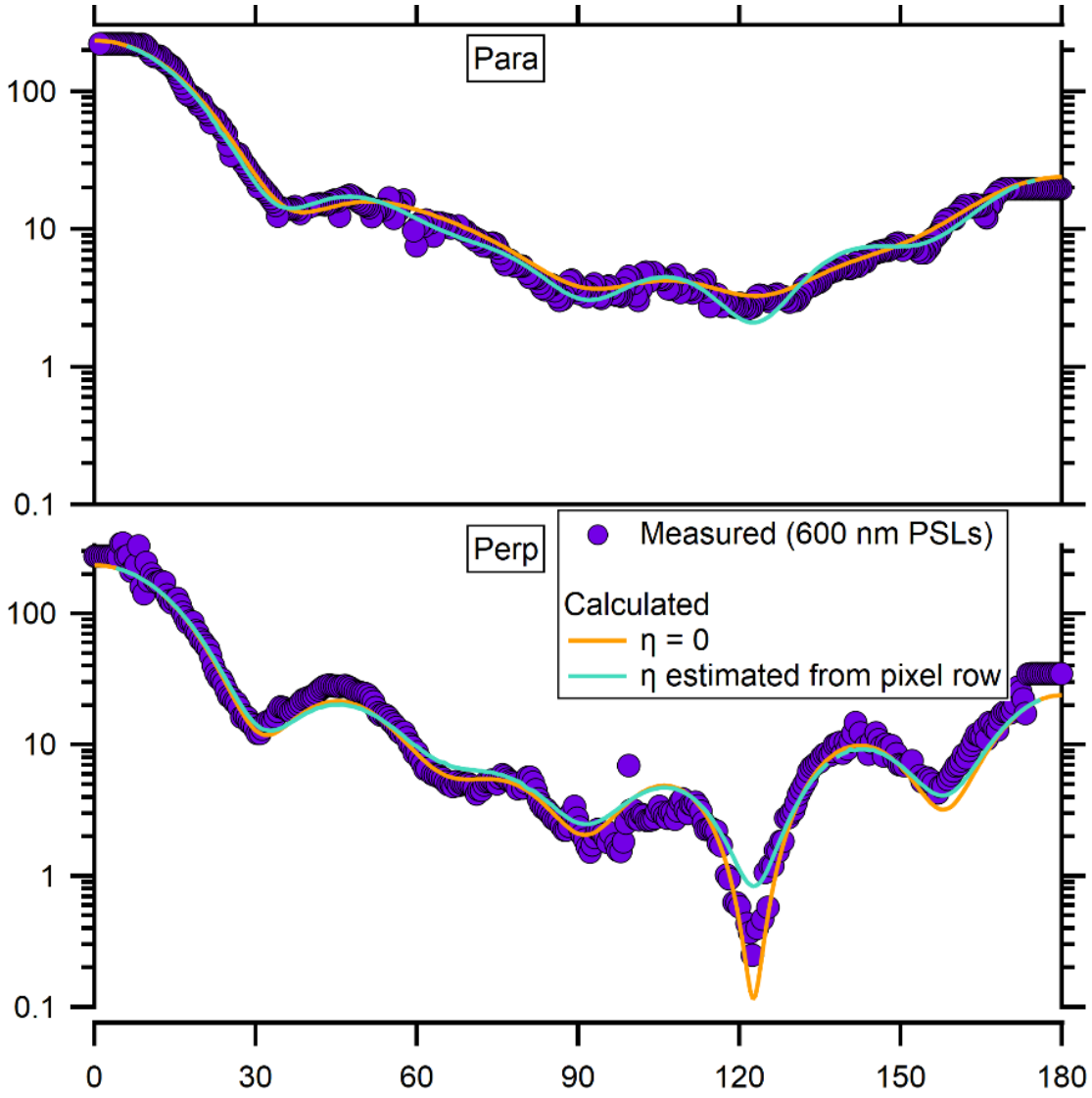

Figure S4. Same as S2 but for λ = 405 nm and PSLs with D_p = 600 nm.

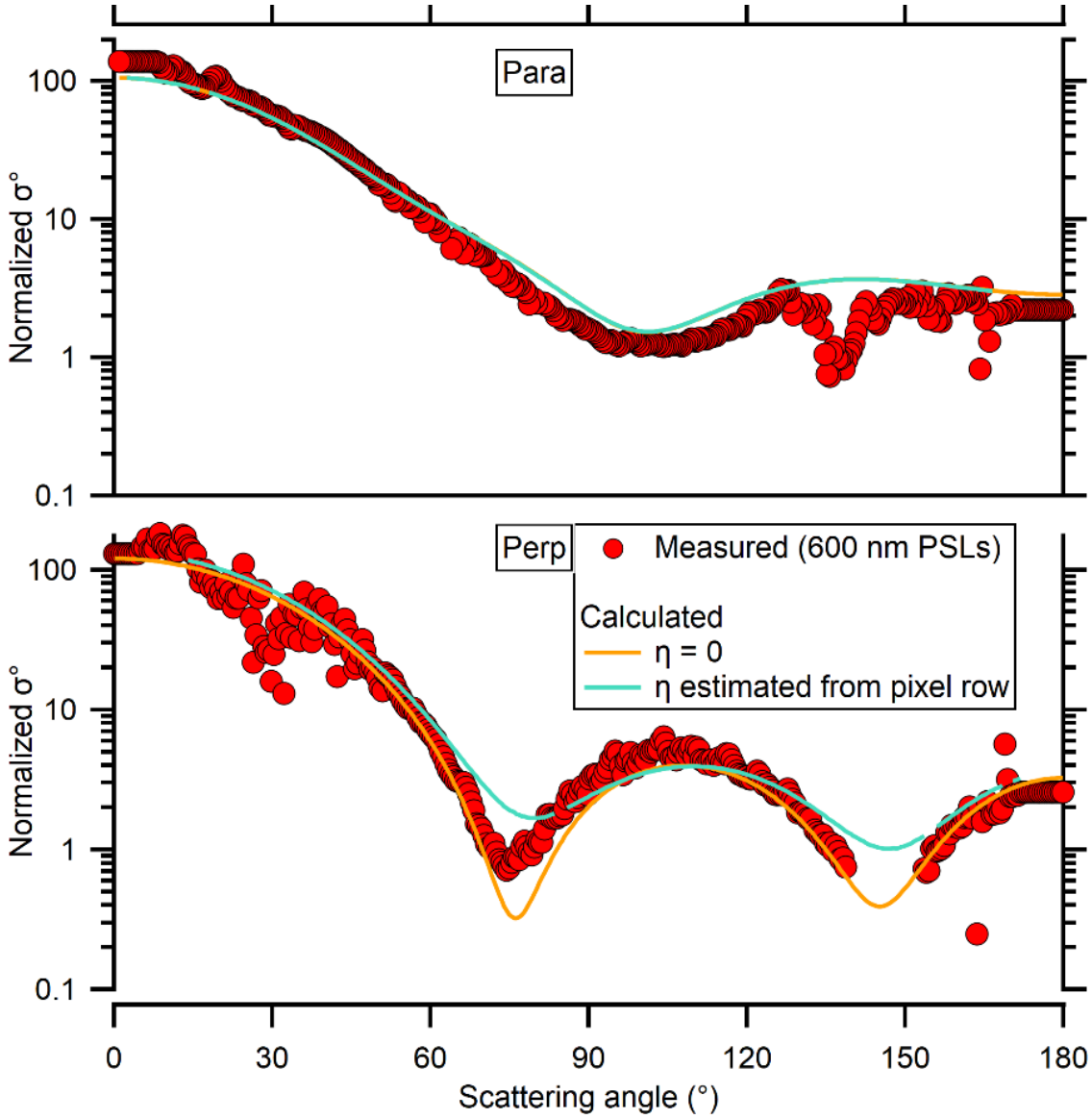

Figure S5. Same as S2 but for λ = 660 nm and PSLs with D_p = 600 nm.

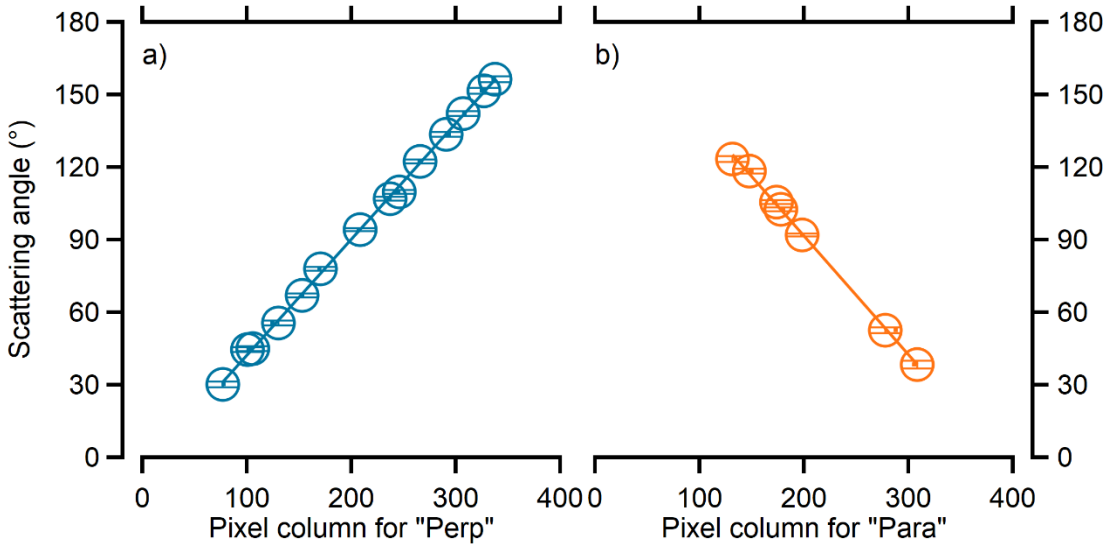

Figure S6. Calibration for converting pixel column to scattering angle using local maxima and minima in σ° from PSLs as measured by a) "Perp" and b) "Para" cameras. Markers show maxima and minima from Mie theory as a function of the corresponding pixel column of the measured σ°, with the differential scattering coefficient calibration applied. Error bars indicate the 95% confidence interval from the linear fit. Dots show the pixel column where the maxima/minima would be located in the raw data, without the differential scattering coefficient calibration.

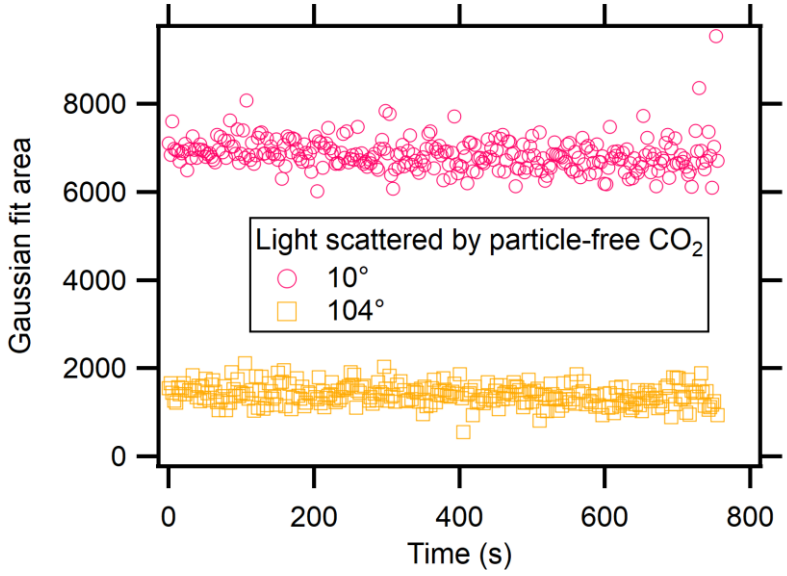

Figure S7. Laser stability shown as area under Gaussian fit for light scattered by CO_2 at two scattering angles. Pink circles and yellow squares show individual measurements of light scattering at 10° and 104°, respectively, as a function of time.

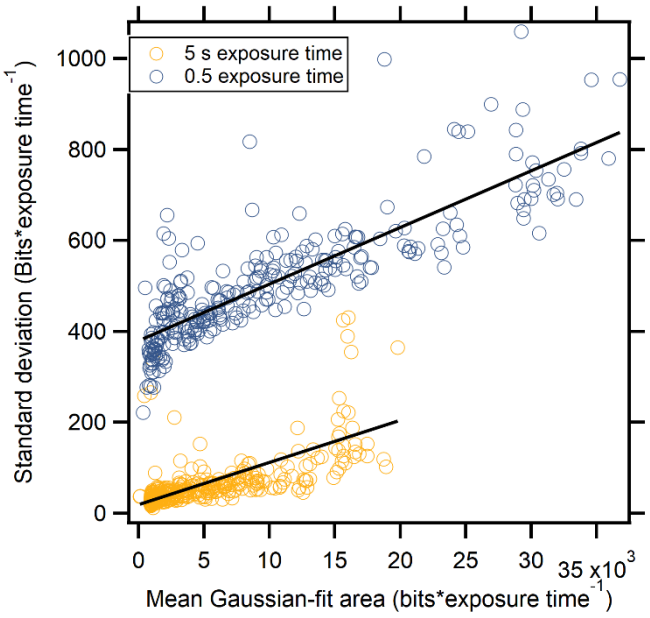

Figure S8. Standard deviation of area under Gaussian fit as a function of the average area under the Gaussian fit for two exposure durations. Each symbol represents a scattering angle for a series of measurements. Black lines are linear regressions fits.

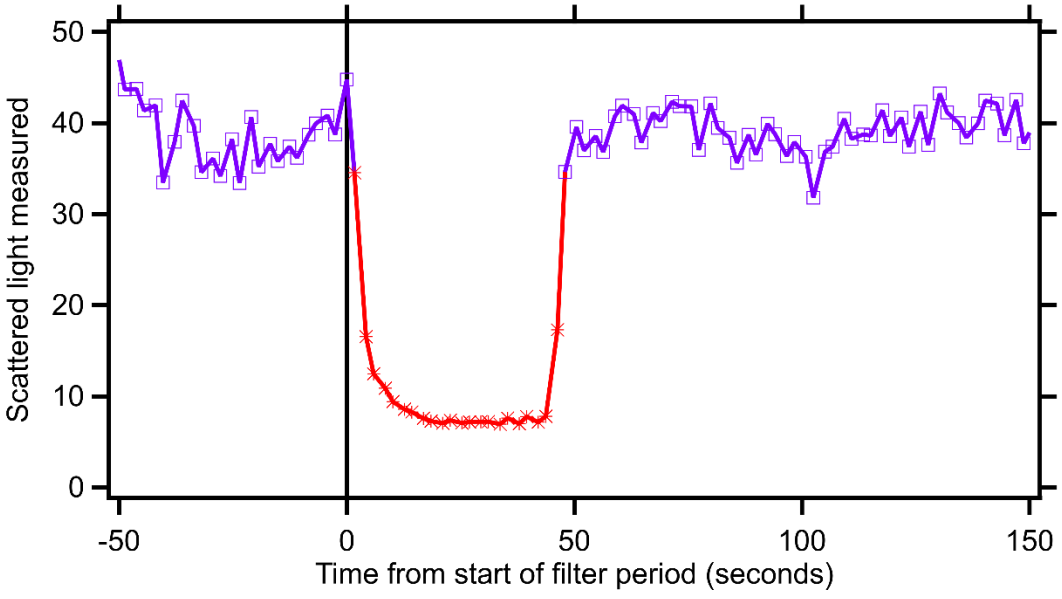

Figure S9. Change in light scattering after inserting a filter during smoke sampling. Red asterisks indicate the filter period and purple squares indicate sample data. Note: only steady-state data from the filter period is used for the subtraction of gas-phase scattering from the sample data.

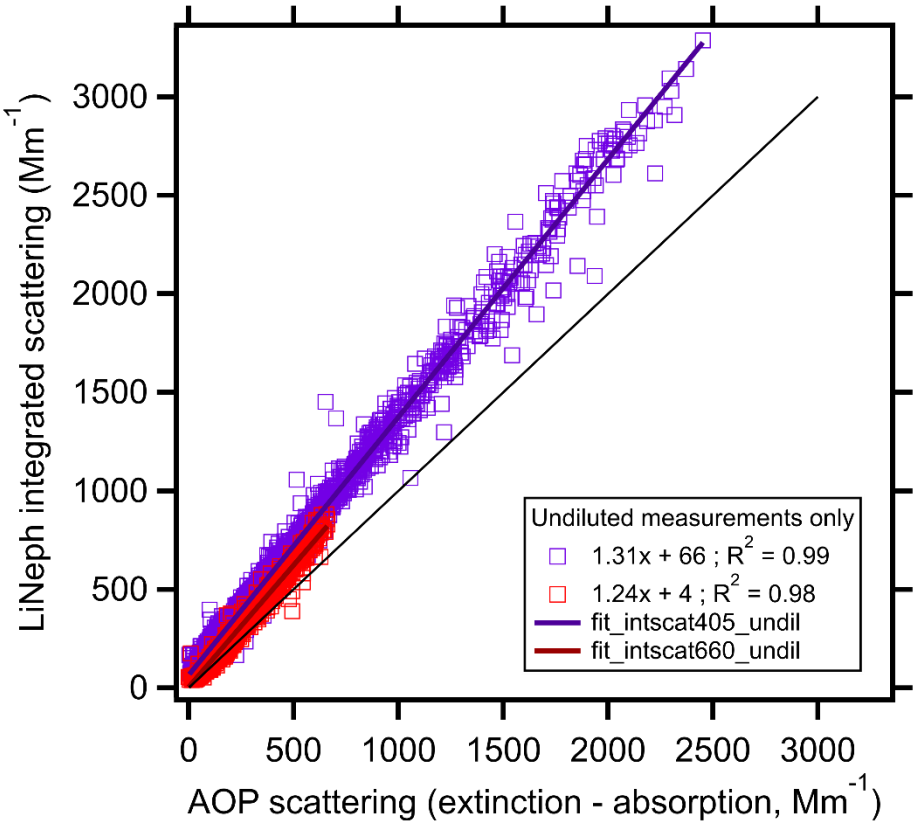

Figure S10. Integrated scattering for undiluted measurements only.

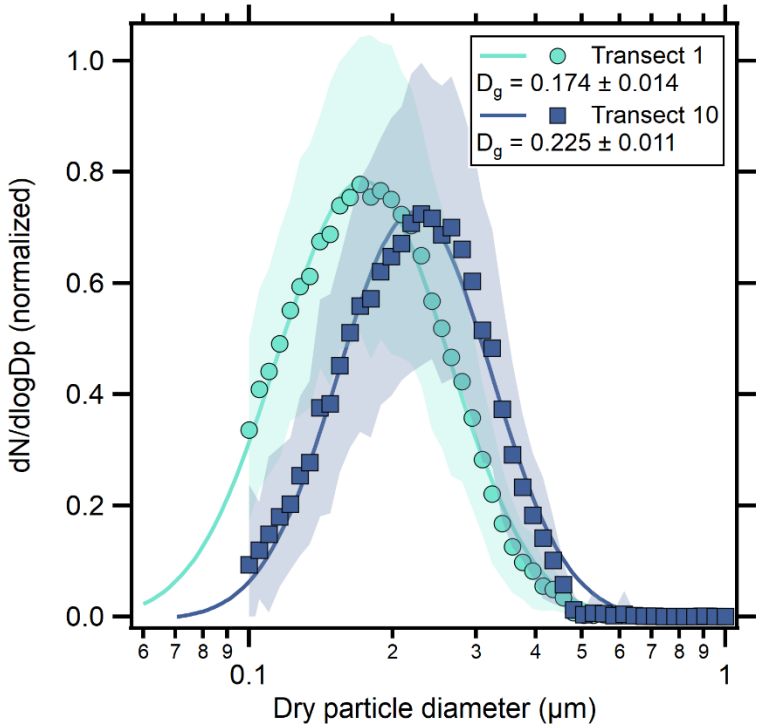

Figure S11. Average normalized particle size distribution for two transects of the Williams Flats fire. Shaded area indicates one standard deviation from the average. The average ± standard deviation geometric mean diameter (D_g) is calculated from lognormal fits of each measured size distribution during each transect.

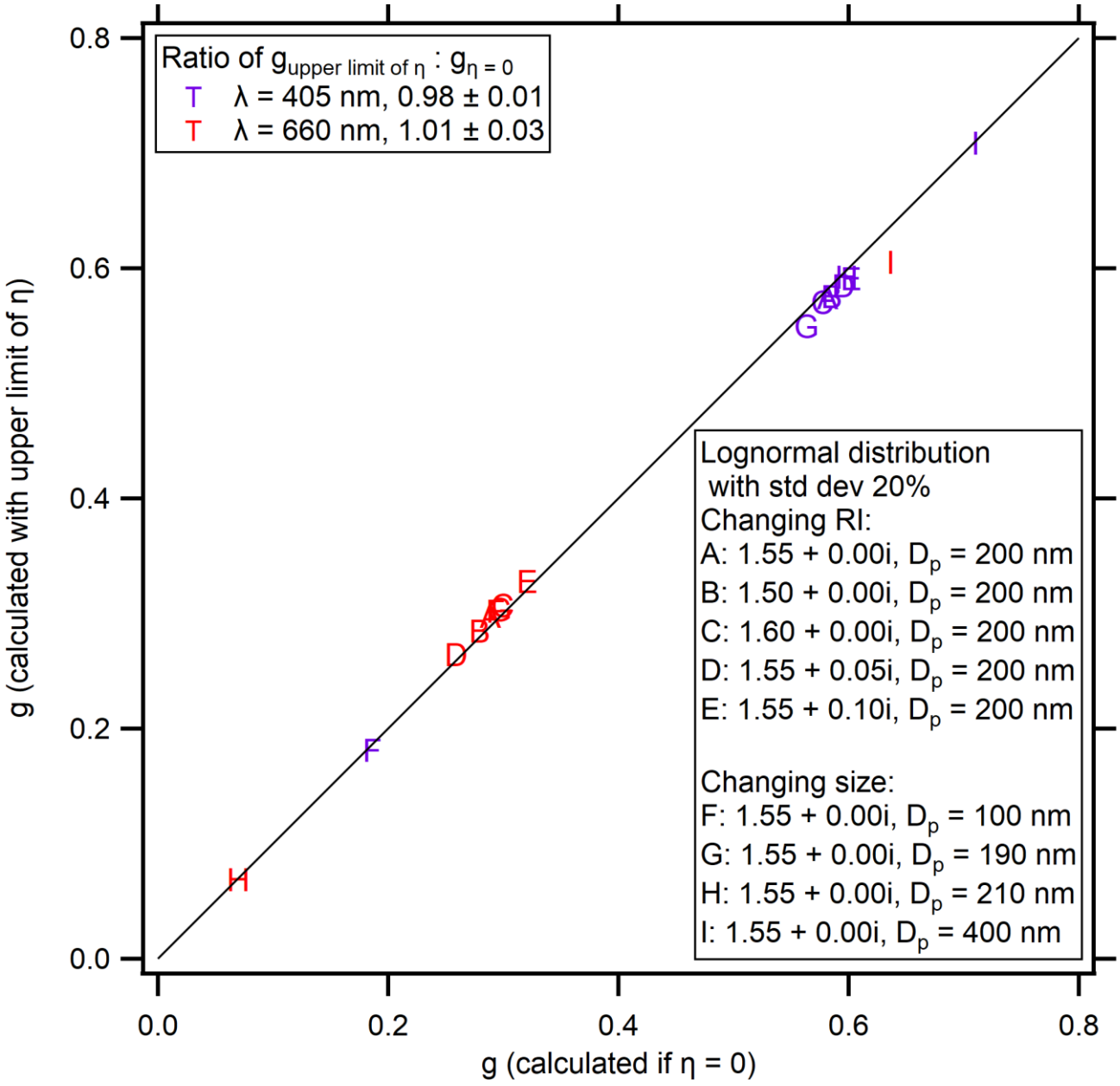

Figure S12. Asymmetry parameter (g) calculated for theoretical aerosol populations. The populations vary in the assumed complex refractive indices and the mode of the lognormal polydisperse size distribution. The x-axis shows the g expected to be measured if η = 0. The y-axis shows the g that would be measured by the LiNeph, assuming the estimated η were used to calculated the differential scattering coefficients (σ°), but then η = 0 were used to calculate g.